17. Hendricks, L. C., McClanahan, S. L., McCaffrey, M., Palade, G. E. & Farquhar, M. G. Golgi proteins persist in the tubulovesicular remnants found in Brefeldin A-treated pancreatic acinar cells. *Eur. J. Cell Biol.* **58,** 202–213 (1992).
18. Lippincott-Schwartz, J. *et al.* Microtubule-dependent retrograde transport of proteins into the ER in the presence of brefeldin A suggests an ER recycling pathway. *Cell* **60,** 821–836 (1990).
19. Shima, D. T., Cabrera-Poch, N., Pepperkok, R. & Warren, G. An ordered inheritance strategy for the Golgi apparatus: visualization of mitotic disassembly reveals a role for the mitotic spindle. *J. Cell Biol.* **141,** 955–966 (1998).
20. Cole, N. B., Sciaky, N., Marotta, A., Song, J. & Lippincott-Schwartz, J. Golgi dispersal during microtubule disruption—regeneration of Golgi stacks at peripheral endoplasmic-reticulum exit sites. *Mol. Biol. Cell* **7,** 631–650 (1996).
21. Storrie, B. *et al.* Recycling of Golgi-resident glycosyltransferases through the ER reveals a novel pathway and provides an explanation for nocodazole-induced Golgi scattering. *J. Cell Biol.* **143,** 1505–1521 (1998).
22. Girod, A. *et al.* Evidence for a COP-I-independent transport route from the Golgi complex to the endoplasmic reticulum. *Nature Cell Biol.* **1,** 423–430 (1999).
23. Lippincott-Schwartz, J. *et al.* Brefeldin A's effects on endosomes, lysosomes, and the TGN suggest a general mechanism for regulating organelle structure and membrane traffic. *Cell* **67,** 601–616 (1991).
24. Reaves, B. & Banting, G. Perturbation of the morphology of the trans-Golgi network following Brefeldin A treatment: redistribution of a TGN-specific integral membrane protein, TGN38. *J. Cell Biol.* **116,** 85–94 (1992).
25. Cluett, E. B. & Brown, W. J. Adhesion of Golgi cisternae by proteinaceous interactions: intercisternal bridges as putative adhesive structures. *J. Cell Sci.* **103,** 773–784 (1992).
26. Nilsson, T. *et al.* Kin recognition between medial Golgi enzymes in HeLa cells. *EMBO J.* **13,** 562–574 (1994).
27. Zaal, K. J. *et al.* Golgi membranes are absorbed into and reemerge from the ER during mitosis. *Cell* **99,** 589–601 (1999).
28. Rowe, T. & Balch, W. E. Expression and purification of mammalian Sar1. *Methods Enzymol.* **257,** 49–53 (1995).
29. Seemann, J., Jokitalo, E. J. & Warren, G. The role of the tethering proteins p115 and GM130 in transport through the Golgi apparatus *in vivo*. *Mol. Biol. Cell* **11,** 635–645 (2000).

Acknowledgements

We would like to thank J. Shorter for his comments. This work was funded by the NIH and J.S. was supported by a postdoctoral fellowship from the Deutsche Forschungsgemeinschaft.

Correspondence and requests for materials should be addressed to G.W. (e-mail: graham.warren@yale.edu).

Steps and fluctuations of *Listeria monocytogenes* during actin-based motility

Scot C. Kuo & James L. McGrath

Department of Biomedical Engineering, The Johns Hopkins University, 720 Rutland Avenue, Baltimore, Maryland 21205, USA

The actin-based motility of the bacterium, *Listeria monocytogenes*, is a model system for understanding motile cell functions involving actin polymerization[1]. Although the biochemical and genetic aspects of *Listeria* motility have been intensely studied[2–5], biophysical data are sparse[6]. Here we have used high-resolution laser tracking to follow the trailing ends of *Listeria* moving in the lamellae of COS7 cells. We found that pauses during motility occur frequently and that episodes of step-like motion often show pauses spaced at about 5.4 nm, which corresponds to the spatial periodicity of F-actin[7]. We occasionally observed smaller steps (<3 nm), as well as periods of motion with no obvious pauses. Clearly, bacteria do not sense cytoplasmic viscoelasticity because they fluctuate 20 times less than adjacent lipid droplets. Instead, bacteria bind their own actin 'tails', and the anchoring proteins can 'step' along growing filaments within the actin tail. Because positional fluctuations are unusually small, the forces of association and propulsion must be very strong. Our data disprove the brownian ratchet model[8] and limit alternative models, such as the 'elastic' brownian ratchet[9] or the 'molecular' ratchet[4,10].

To monitor the motions of *Listeria* in living cells, we adapted a high-resolution laser-based device originally developed for spherical particles in optical tweezers. Such devices use split photodiode detectors to monitor forward-scattered laser light, often from the trapping laser[11–15]. Our device avoids optical forces by using extremely low optical power (<0.15 mW) and uses a quadrant photodiode detector to provide two-dimensional (2D) tracking. This device provided the basis of a new approach, called laser-tracking microrheology, to measure the viscoelastic moduli of polymeric solutions and of subcellular regions in living cells[16–18]. To adapt the device for rod-shaped bacteria, we mapped the optical response while performing a 2D raster scan of fixed bacteria (Fig. 1). Unlike spherical particles, the position of highest signal sensitivity was not at the centre of bacteria, but at the centre of their hemispherical ends. Furthermore, laser-tracking signals were non-linear with position and depended on bacterial orientation relative to the axes of the quadrant photodiode detector. To account for these effects, we perform automated 2D raster calibrations with the piezostage before every high-resolution acquisition.

Data from tracking the actin-based motility of *Listeria* in lamellae of living COS7 cells are shown in Fig. 2. By automated repositioning of the piezostage, we followed the trailing end of a bacterium for 2 min and acquired high-resolution data at each piezostage position (Fig. 2b). Two features are apparent from these trajectories (Fig. 2c). First, bacterial fluctuations are very small; across all 20 high-resolution trajectories, bacterial fluctuations are 1.31 ± 0.04 nm and 0.94 ± 0.03 nm (mean r.m.s. ± s.e.m.) in the directions parallel and perpendicular to movement, respectively. Second, pauses greater than 50 ms are common during motility and appear in 85% of these 1-s trajectories. Despite hundreds of filaments and fast motility, episodes of step-like progress are common and pauses are often spaced about 5.4 nm apart (Fig. 2c). These steps are considerably smaller than the micrometre-scaled episodic motion observed in certain *Listeria* mutants[3,19]. Spatial frequencies can be analysed using histograms of all pairwise displacements[20] followed by Fourier transform analysis of histograms[12] (Fig. 2d, e). Such analysis of the data in Fig. 2c shows only spatial frequencies of 0.18 nm^{-1} (5.5 nm) and no evidence for higher harmonics (for example, 2.7 nm). In other trajectories, a spacing of 5–6 nm between pauses is dominant in positional histograms, although smaller steps (~3 nm) are

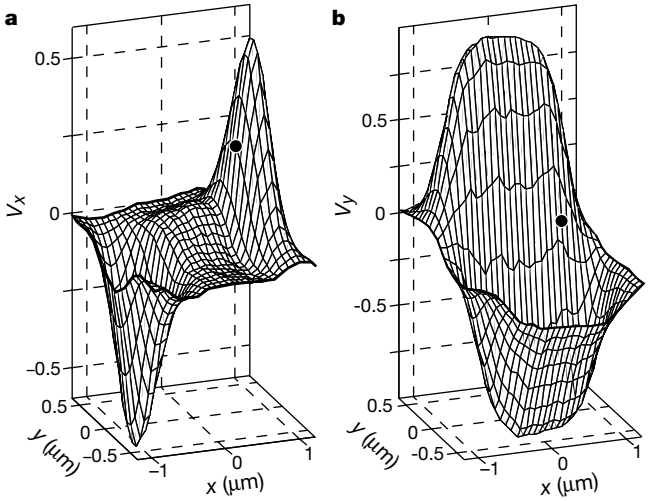

Figure 1 Response of laser-tracking signals with bacterial position. Dead bacteria were adsorbed to glass coverslips and scanned with a 2D raster pattern in 75-nm steps with the piezostage. Voltage signals are shown parallel (V_x) (**a**) and perpendicular (V_y) (**b**) to the bacterium's long axis. The dot represents unique (V_x, V_y) signals that would be used by software to position the piezostage to track motion in the $-x$ direction. For live-cell tracking, calibrations patterns are much smaller (see Methods).

detectable. These features persist in instances of faster motility (see the 7 μm min^{-1} example in Supplementary Information). In general, noise in positional measurements (1.9 ± 0.9 nm, mean r.m.s. ± s.d.) can obscure short-lived steps of about 2.5 nm that may occur in episodes of apparently continuous movement. The ~5.4-nm spacing corresponds to the size of G-actin and to the spatial periodicity of F-actin[7] (the significance of which will be discussed below).

Because fluctuations can reveal local mechanical properties, we show that fluctuations in positional measurements are largely due to the optical fluctuations of surrounding lamellae (Fig. 3). On exposure to *Listeria*, all cells show increased optical fluctuations in their lamellae, even when bacteria are not internalized. This may be due to bacterial secretion of listeriolysin O, a pore-forming cytolysin, into the culture media (D. A. Portnoy, personal communication). To estimate an upper bound for the magnitude of brownian fluctuations of *Listeria*, we note that all fluctuation measurements in Fig. 3 have standard errors of less than 0.04 nm (~3%). To be indistinguishable ($P > 0.95$) from the interfering background signals, the addition of *Listeria* fluctuations must be within two standard errors. Hence, an initial estimate of *Listeria* fluctuations is less than 0.1 nm (2.5 × s.e.m.), which is smaller than a covalent bond. Clearly, molecules on the surface of moving *Listeria* can fluctuate much more than the whole bacterium.

No comparable organelle in COS7 shows such small fluctuations. Because they are relatively rigid and distribute throughout COS7 cells, lipid droplets make ideal probes for comparing subcellular mechanics[17]. Lipid droplets fluctuate the least (9.9 nm) in lamellae, making lamellae the most rigid region of cytoplasm[17]. Even when compensating for their larger size and shape, motile *Listeria* fluctuate at least 20-fold less than is expected from lipid droplets near the bacterium's path (Fig. 4). Because bacteria do not 'sense' the local cytoplasmic viscoelasticity, they must be tightly associated to their actin 'tails'. From studies of reconstituted *Listeria* motility in extracts, theoretical implications of the medium's low viscosity[21] and direct 'plucking' with optical tweezers[22] also argue for tail binding by bacteria. By the equipartition principle[23], the small brownian fluctuations of bacteria ($\langle \Delta x^2 \rangle < 0.1\ \mathrm{nm}^2$) indicate strong tethering forces with an apparent spring constant, $\kappa = k_B T / \langle \Delta x^2 \rangle > 40\ \mathrm{pN\ nm}^{-1}$, where k_B is Boltzmann's constant and T is absolute temperature. If such tail-binding remained constant, then more than 220 pN of force ($F = \kappa s$) would be needed to make a step (s = 5.4 nm).

The brownian ratchet model[8] makes specific predictions of bacterial fluctuations. In this model, F-actin does not flex and positional fluctuations of bacteria must be large enough to allow intercalation of G-actin (>2.7 nm) at appropriate timescales. To evaluate fluctuations, we calculate a mean-squared residual-displacement (MSrD; see Methods) where linear trends are removed before statistical analysis. Like the more traditional mean-squared displacement (MSD) analysis[24], MSrD measures the extent of diffusive motion at different timescales. Unlike the MSD, however, MSrD analyses of the brownian ratchet model are not quadratic functions of lag time (τ), but are generally linear functions that show the magnitude of diffusion. At longer lag times ($\tau \approx T/2$, where T is the duration of each simulated trajectory), MSrD(τ) reaches a maximum because numerical detrending necessarily removes the slower diffusive components of the brownian ratchet. From MSrD(τ) analysis of *Listeria* motion (Fig. 4), it is clear that the diffusive component of brownian ratchet motions should have been detectable despite the large optical fluctuations of the lamellae. Compared with velocity-matched simulations of the brownian ratchet (1.2 μm min^{-1} for Fig. 4), fluctuations of bacteria are markedly different ($P < 0.005$).

These data directly contradict the brownian ratchet model in four ways. First, fluctuations of bacteria are much smaller than the intercalation size of G-actin. Our best estimates are less than 0.1 nm. Second, MSrD(τ) analysis suggests that bacteria do not diffuse according to predictions from brownian ratchet simulations. Third, because bacteria fluctuate 20 times less than adjacent particles, bacteria bind their actin 'tails'. Indeed, when motility occasionally stops, bacteria can detach from their tails and show extremely large fluctuations, including 'fish-tailing' (see movie in Supplementary Information). Last, because *Listeria* have episodes of motility with pauses spaced at about 5.4 nm, the bacteria probably step along growing actin filaments. Because hundreds of filaments are in the actin tail, it is remarkable that these episodes of step-like progress occur. Either progress along many filaments is coordinated, or attachment to only a few filaments, perhaps those stretched under the greatest tension, limits bacterial motility.

The discovery that *Listeria* can make steps at the spatial periodicity of F-actin critically modifies remaining models of *Listeria*

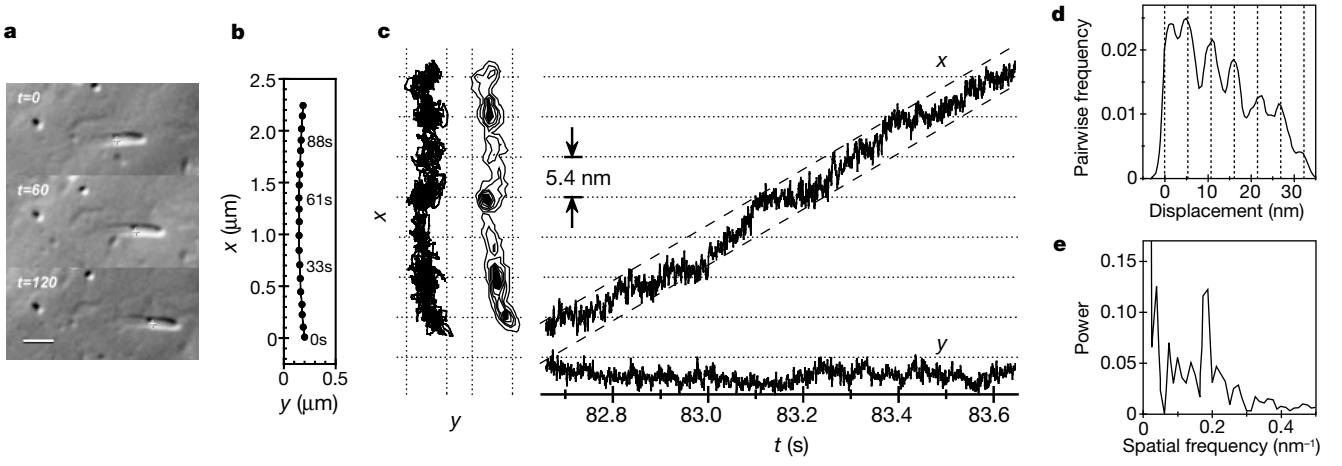

Figure 2 Actin-based motility in COS7 lamellae. **a**, Video-enhanced differential-interference contrast images of motility (laser focused at crosses; scale bar, 2 μm). **b**, Piezostage coordinates for each high-resolution acquisition (overall speed 1.2 μm min^{-1} along x). **c**, High-resolution trajectory with many pauses (x, r.m.s. 1.5 nm; linear-fit slope 2.3 μm min^{-1}). Left, the bacterium's trajectory and a contour plot of its positional frequencies (bins 0.75 × 0.75 nm; local maxima >20 ms nm^{-2} filled black) with transposed axes. Right, bacterial position versus time. All grid lines are spaced at 5.4 nm, and dashed lines denote the intercalation size for G-actin (linear fit ±2.7 nm). **d**, **e**, Spatial frequency analysis of step size. **d**, Normalized histogram of pairwise displacements. For the positional data of **c**, histogram (bins 0.5 nm) of displacements between all pairs of coordinates show a strong 5.4-nm periodicity (grid spacing 5.4 nm). **e**, Fourier analysis (power spectrum) of pairwise displacement histogram in **d** show only 0.18 nm^{-1} (5.5 nm) and no higher spatial frequencies.

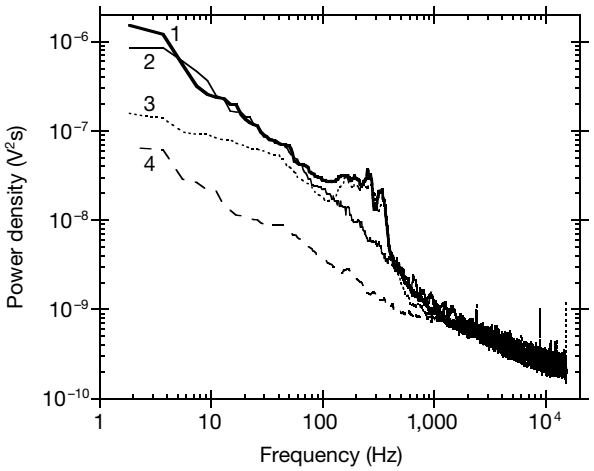

Figure 3 Power spectra of laser-tracking signals. Voltage fluctuations of moving *Listeria* (1); empty lamellae within 2 μm of moving bacterium (2); dead bacterium (0.02% azide) embedded in 15% polyacrylamide (3); and cell-free region of specimen (4). Before calculating power spectra, all voltage data were detrended by subtracting any linear moving component. Mechanical resonances (~250 Hz) of the piezostage and microscope are only visible with bacteria. Power spectra from several acquisitions were averaged for this figure, using $n = 40$, 14, 49 and 56 for spectra 1–4, respectively.

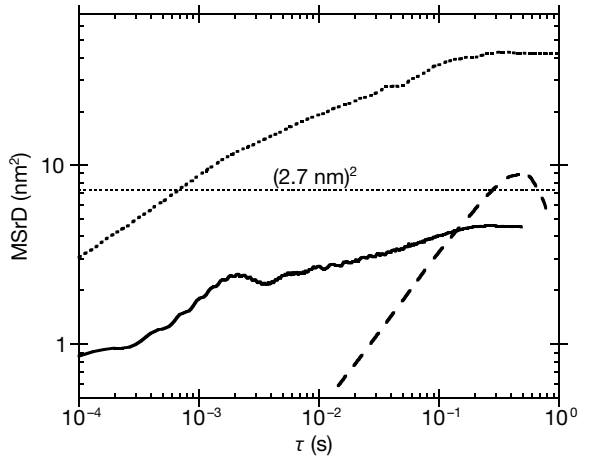

Figure 4 Comparisons of fluctuations. Mean-squared residual displacement (MSrD) was calculated as described in Methods for the motions of adjacent lipid droplet (dotted line); simulation of the brownian ratchet model (dashed line); and actin-based motility of *Listeria* averaged across all acquisitions of Fig. 2b (solid line). Model simulations matched the duration of *Listeria* data sets. For comparison, the intercalation gap for G-actin, 2.7 nm, is drawn as a horizontal, thin dotted line (MSrD = 7.3 nm²).

motility. In the 'elastic' brownian ratchet model[9], bacteria do not bind F-actin and the bending fluctuations of actin filaments allow intercalation of G-actin. From our data, bacteria bind their actin tails and the binding is very restrictive. To observe bacterial steps at the periodicity of F-actin, the ends of bound filaments must fluctuate less than the size of G-actin, hence preventing monomer intercalation by this model. In the 'molecular' ratchet model[4,10], filament growth occurs when the barbed end of F-actin cyclically attaches and detaches from bacterium-bound protein complexes. For the actin-based motility of *Listeria* and *Shigella flexneri*, F-actin binding is mediated by vasodilator-stimulated phosphoprotein (VASP) bound to ActA or neuronal Wiskott–Aldrich syndrome protein (N-WASP) bound to IcsA, respectively[2–4,10]. In the molecular ratchet, tethered filaments are under compression when growing. Just as observed in actomyosin experiments[25–27], however, F-actin will bend under compression, hence shortening, if not obscuring, steps. Many hundred filaments about *Listeria*, and different elongation mechanisms may operate on different filaments.

To show steps at the spatial periodicity of F-actin, bacterial motion is most probably limited by binding to a few filaments that are stretched taut. Unless filaments undergo coordinated growth, longer filaments will be flexed providing 'pressure' and a few tethered filaments become stretched (see Supplementary Information). Probably tethered to the sides of actin filaments by the VASP–ActA protein complex, bacteria 'slip' along these taut filaments to reveal their periodicity of 5.4 nm. If several staggered filaments limit bacterial motility, steps could be smaller and have uneven spacing. Reminiscent of molecular motors, stepping requires some processivity of the tethering proteins along the taut filaments as they grow. Otherwise, long periods of dissociation would skip or obscure steps, particularly when taut filaments relax. Analogies to molecular motors will probably guide future biophysical studies of the actin-based motility of *Listeria*. □

Methods

Host cells and infections

We tried using J774 macrophages as hosts for *Listeria* infections[28], but J774 cells spread poorly. Thick cells were rich with organelles that confused laser-tracking signals, and the minority of well-spread J774 cells seemed to resist *Listeria* infection. We therefore used the kidney-derived COS7 cell line (ATCC CRL-1651) in which we previously measured subcellular mechanical properties[17]. Although COS7 cells are not as readily infected as J774 macrophages, *Listeria* can infect cells with well-spread lamellae and can move on actin-rich tails that stain with fluorescent phalloidin (data not shown).

We grew and maintained virulent *L. monocytogenes* (strain 10403S)[28] and COS7 cells[17] as described. We modified these protocols for infection and microscopy by using CO_2-independent Leibovitz's L15 medium (Life Technologies) supplemented with 10% fetal bovine serum. After 1 h of infection (multiplicity of infection, MOI = 370) in this medium, excess bacteria were removed by extensive washing and infected cells were allowed to grow for 3 h in medium supplemented with 5 μg ml^{-1} gentamicin to kill free-swimming bacteria[28]. We carried out all infections and growth at 37 °C, and all microscopy and laser tracking at room temperature (23 °C).

Laser tracking and data analysis

During experiments, automated software cyclically repeated the following sequence: trailing ends of bacteria were placed at the laser focus (Fig. 1) by moving the piezostage (Queensgate Instruments); laser-tracking signals were calibrated with a 2D raster scan spanning 240 nm in 30-nm steps; and high-resolution position data (30 kHz) were recorded with the piezostage stationary. Except for power spectra (Fig. 3), we reduced electro-optical noise by digital filtering with a 5-kHz cut-off, subsampled at 10 kHz, and median filtered in a sliding window of 0.9 ms. Using corresponding raster calibrations, 2D interpolation (MatLab; MathWorks) converted laser-tracking signals into positions. After removing the linear trend in a trajectory $x(t)$, we calculated r.m.s. values by r.m.s. $= \sqrt{(\Sigma x^2/N)}$ for N positions over the whole duration, T, of the high-resolution trajectory. Also starting with detrended $x(t)$, we calculated the mean-squared residual displacement (MSrD) as a function of lag time, τ, by $\mathrm{MSrD}(\tau) = \Sigma[x(t+\tau) - x(t)]^2/n$ for all possible n pairs of positions ($n < N$). For spatial frequency analysis (Fig. 2d), trajectories were first median filtered with a window of 3.5 ms. We calculated displacements as $(x(t_2) - x(t_1))$ for all data pairs $t_2 > t_1 \geq 0$, and histograms of these displacements were normalized by the total number of pairwise displacements, $N(N-1)/2$ (ref. 20). We calculated the one-sided power spectrum (Fig. 2e) from the pairwise displacements histogram, with negative displacements excluded[12]. For Fig. 4, simulations of the ideal brownian ratchet used step size $\delta = 2.7$ nm and diffusion coefficient $D = 28$ nm^2 s^{-1} so that the average velocity is 1.2 μm min^{-1} (ref. 8). We calculated the simulation with 0.2-ms temporal resolution, and we calculated MSrD as described for moving *Listeria*.

Received 20 April; accepted 22 August 2000.

1. Borisy, G. G. & Svitkina, T. M. Actin machinery: pushing the envelope. *Curr. Opin. Cell Biol.* **12,** 104–112 (2000).
2. Smith, G. A., Theriot, J. A. & Portnoy, D. A. The tandem repeat domain in the *Listeria monocytogenes* ActA protein controls the rate of actin-based motility, the percentage of moving bacteria, and the localization of vasodilator-stimulated phosphoprotein and profilin. *J. Cell Biol.* **135,** 647–660 (1996).
3. Lasa, I. *et al.* Identification of two regions in the N-terminal domain of ActA involved in the actin comet tail formation by *Listeria monocytogenes*. *EMBO J.* **16,** 1531–1540 (1997).
4. Laurent, B. *et al.* Role of proteins of the Ena/VASP family in actin-based motility of *Listeria monocytogenes*. *J. Cell Biol.* **144,** 1245–1258 (1999).
5. Loisel, T. P., Boujemaa, R., Pantaloni, D. & Carlier, M. -F. Reconstitution of actin-based motility of *Listeria* and *Shigella* using pure proteins. *Nature* **401,** 613–615 (1999).
6. Theriot, J. A. The polymerization motor. *Traffic* **1,** 19–28 (2000).
7. Holmes, K. C., Popp, D., Gebhard, W. & Kabsch, W. Atomic model of the actin filament. *Nature* **347,** 44–49 (1990).
8. Peskin, C., Odell, G. & Oster, G. Cellular motions and thermal fluctuations: the Brownian ratchet. *Biophys. J.* **65,** 316–324 (1993).
9. Mogilner, A. & Oster, G. Cell motility driven by actin polymerization. *Biophys. J.* **71,** 3030–3045 (1996).
10. Egile, C. *et al.* Activation of the CDC42 effector N-WASP by the *Shigella flexneri* IcsA protein promotes actin nucleation by Arp2/3 complex and bacterial actin-based motility. *J. Cell Biol.* **146,** 1319–1332 (1999).

11. Denk, W., Webb, W. W. & Hudspeth, A. J. Mechanical properties of sensory hair bundles are reflected in their Brownian motion measured with a laser differential interferometer. *Proc. Natl Acad. Sci. USA* **86,** 5371–5375 (1989).
12. Svoboda, K., Schmidt, C. F., Schnapp, B. J. & Block, S. M. Direct observation of kinesin stepping by optical trapping interferometry. *Nature* **365,** 721–727 (1993).
13. Kojima, H., Muto, E., Higuchi, H. & Yanagida, T. Mechanics of single kinesin molecules measured by optical trapping nanometry. *Biophys. J.* **73,** 2012–2022 (1997).
14. Allersma, M. W., Gittes, F., deCastro, M. J., Stewart, R. J. & Schmidt, C. F. Two-dimensional tracking of ncd motility by back focal plane interferometry. *Biophys. J.* **74,** 1074–1085 (1998).
15. Pralle, A., Prummer, M., Florin, E. L., Stelzer, E. H. & Horber, J. K. Three-dimensional high-resolution particle tracking for optical tweezers by forward scattered light. *Microsc. Res. Tech.* **44,** 378–386 (1999).
16. Mason, T. G., Ganesan, K., Van Zanten, J. H., Wirttz, D. & Kuo, S. C. Particle tracking microrheology of complex fluids. *Phys. Rev. Lett.* **79,** 3282–3285 (1997).
17. Yamada, S., Wirtz, D. & Kuo, S. C. Mechanics of living cells measured by laser tracking microrheology. *Biophys. J.* **78,** 1736–1747 (2000).
18. McGrath, J. L., Hartwig, J. H. & Kuo, S. C. The mechanics of F-actin microenvironments depend on the chemistry of probing surfaces. *Biophys. J.* (in the press) (2000).
19. Gerbal, F. *et al.* On the 'Listeria' propulsion mechanism. *Pramana. J. Phys.* **53,** 155–170 (1999).
20. Kuo, S. C., Gelles, J., Steuer, E. & Sheetz, M. P. A model for kinesin movement from nanometer-level movements of kinesin and cytoplasmic dynein and force measurements. *J. Cell Sci.* **14** (suppl.)**,** 135–138 (1991).
21. Olbris, D. J. & Herzfeld, J. Reconstitution of *Listeria* motility: implications for the mechanism of force transduction. *Biochim. Biophys. Acta* **1495,** 140–149 (2000).
22. Gerbal, F. *et al.* Measurement of the elasticity of the actin tail of *Listeria monocytogenes*. *Eur. Biophys. J.* **29,** 134–140 (2000).
23. Reif, F. *Fundamentals of Statistical and Thermal Physics* (McGraw-Hill, New York, 1965).
24. Qian, H., Sheetz, M. P. & Elson, E. L. Single particle tracking: Analysis of diffusion and flow in two-dimensional systems. *Biophys. J.* **60,** 910–921 (1991).
25. Molloy, J. E., Burns, J. E., Kendrick-Jones, J., Tregear, R. T. & White, D. C. Movement and force produced by a single myosin head. *Nature* **378,** 209–212 (1995).
26. Mehta, A. D., Finer, J. T. & Spudich, J. A. Detection of single molecule interactions using correlated thermal diffusion. *Proc. Natl Acad. Sci. USA* **94,** 7927–7931 (1997).
27. Dupuis, D. E., Guilford, W. H., Wu, J. & Warshaw, D. M. Actin filament mechanics in the laser trap. *J. Muscle Res. Cell Motil.* **18,** 17–30 (1997).
28. Portnoy, D. A., Jacks, P. S. & Hinrichs, D. J. Role of hemolysin for the intracellular growth of *Listeria monocytogenes*. *J. Exp. Med.* **167,** 1459–1471 (1988).

Supplementary information is available on *Nature*'s World-Wide Web site (http://www.nature.com) or as paper copy from the London editorial office of *Nature*.

Acknowledgements

We thank L. Machesky for J774 cells, and D. Portnoy and J. Skoble for *Listeria* strains and general advice. We also thank the National Science Foundation, the National Institutes of Health and the Whitaker Foundation for their support. J.L.M. was supported as a BME Distinguished Postdoctoral Fellow, partially funded by the Whitaker Foundation.

Correspondence and requests for materials should be addressed to S.C.K. (e-mail: skuo@bme.jhu.edu).

Crystal structure of fibroblast growth factor receptor ectodomain bound to ligand and heparin

Luca Pellegrini*, David F. Burke*, Frank von Delft*, Barbara Mulloy† & Tom L. Blundell*

** Department of Biochemistry, University of Cambridge, 80 Tennis Court Road, Cambridge, CB2 1GA, UK*
† National Institute for Biological Standards and Control, South Mimms, Potters Bar, EN6 3QG, UK

Fibroblast growth factors (FGFs) are a large family of structurally related proteins with a wide range of physiological and pathological activities[1]. Signal transduction requires association of FGF with its receptor tyrosine kinase (FGFR)[2] and heparan sulphate proteoglycan in a specific complex on the cell surface. Direct involvement of the heparan sulphate glycosaminoglycan polysaccharide in the molecular association between FGF and its receptor is essential for biological activity[3–5]. Although crystal structures of binary complexes of FGF–heparin[6,7] and FGF–FGFR[8,9] have been described, the molecular architecture of the FGF signalling complex has not been elucidated. Here we report the crystal structure of the FGFR2 ectodomain in a dimeric form that is induced by simultaneous binding to FGF1 and a heparin decasaccharide. The complex is assembled around a central heparin molecule linking two FGF1 ligands into a dimer that bridges between two receptor chains. The asymmetric heparin binding involves contacts with both FGF1 molecules but only one receptor chain. The structure of the FGF1–FGFR2–heparin ternary complex provides a structural basis for the essential role of heparan sulphate in FGF signalling.

We reconstituted the ligand-binding extracellular region of human FGFR2 (splice variant IIIc) as a ternary complex with human FGF1 and a heparin decasaccharide by mixing the three components in a 2:2:1 stoichiometric ratio. The ternary complex eluted as a single peak at the expected relative molecular mass of 83,600 (M_r 83.6K) on size-exclusion chromatography. The complex was crystallized and its structure determined by X-ray crystallography at 2.8 Å using multiple anomalous dispersion based on selenomethionine substitution of the receptor moiety (Table 1).

Analysis of the crystals shows that one heparin decasaccharide links two FGF1 molecules, each of which binds a receptor ectodomain, unambiguously defining a heteropentameric assembly, consistent with the *in vitro* reconstitution (Fig. 1a, b). The complex can alternatively be considered as two 1:1 FGF1–FGFR2 complexes associated through interaction with the heparin. The ligand-binding fragment of FGFR2 comprises two immunoglobulin-like domains, D2 (residues 152–249) and D3 (residues 254–360), separated by a short linker (residues 250–253)[8,9] (Fig. 1c). D2 belongs to the I class, whereas D3 approximates to a class C2 fold. FGF1 adopts the well-characterized β-trefoil fold[10]. The two receptor chains in the ternary complex show marked bends in the linker regions, with angles of 106° and 87° between D2 and D3. The two protein halves of the complex are related by an approximate two-fold symmetry axis, which we expect would lie perpendicular to the membrane in the cell. The root-mean square deviation (r.m.s.d.) for the Cα superposition of the two halves of the complex is 2.8 Å, whereas the r.m.s.d. for the 230 Cα atoms of FGF1 and D2 is 1.0 Å.

There are two 1:1 FGF–FGFR binary complexes within the heteropentamer, which we refer to as A and B. In A both ligand and receptor interact with heparin, whereas in B only the ligand is in contact with heparin. The entire length of the protein-bound heparin decasaccharide is visible in the experimental electron-density map (Fig. 2a). Heparin lies between and interacts with the two FGF1 molecules, but is tilted away from the quasi-dyad so that it extends past the ligand dimer to interact only with receptor ectodomain A (Figs 1a, b and 3a). The heparin helix presents a marked distortion that has not been observed in previous structural studies of FGF–heparin complexes[6,7]. The helical axis shows a 34° kink between disaccharides 2 and 3, accompanied by a decreased helical rise between disaccharide 2 and 3 (7.1 Å) and between 3 and 4 (7.9 Å) (for numbering of heparin disaccharide units see Fig. 2b). The total surface area buried at the protein–heparin interface is large at 2,240 Å^2 (617 Å^2 with FGF1 and 631 Å^2 with domain D2 in A; 992 Å^2 with FGF1 in B). van der Waals contacts contribute substantially to the protein–heparin interactions as suggested previously[11]. FGF1 binding to heparin is mediated by a set of basic and polar residues, Asn 18, Lys 112, Lys 113, Asn 114, Lys 118, Arg 119, Arg 122, Gln 127 and Lys 128, which were identified in previous structural and mutagenesis experiments[6,7,11]. FGF1 in binary complex A interacts with six monosaccharides, from iduronic acid in disaccharide 1 (IdoA-1) to glucosamine in disaccharide 4 (GlcN-4), whereas FGF1 in B interacts with five monosaccharides, from GlcN-1 to GlcN-3 (Fig. 2b).

In the structure of the ternary complex, heparin links two FGF1 molecules into a dimer that lacks a protein–protein interface, in a